RSC Advances

PAPER

View Article Online
View Journal | View Issue

Check for updates

Cite this: RSC Adv., 2017, 7, 34705

Received 4th February 2017
Accepted 9th June 2017

DOI: 10.1039/c7ra01444a

rsc.li/rsc-advances

Ag_3PO_4@holmium phosphate core@shell composites with enhanced photocatalytic activity

Fengfeng Li,[ab] Zhihong Li,*[a] Mingxi Zhang,[cb] Yi Shen,*[b] Yongfeng Cai,[b] Yaran Li,[b] Xinyu He[b] and Chen Chen[b]

In this study, Ag_3PO_4@holmium phosphate (HP) composite photocatalysts were first prepared by silver-ammonia-solution-assisted solution co-deposition. During co-deposition, Ag_3PO_4 particles were encapsulated by a flocculent amorphous substance layer of HP, affording a Ag_3PO_4@HP core–shell heterojunction structure with a Ho/Ag molar ratio of 0.05/2.95. The core–shell structure significantly improved the photocatalytic activity of Ag_3PO_4. In addition, the photocatalytic mechanism of Ag_3PO_4@HP was discussed.

1. Introduction

Semiconductor photocatalysts have attracted considerable attention as they demonstrate the potential of addressing energy and environmental issues,[1–4] including photochemical water splitting,[5] organic pollutant degradation,[6] and CO_2 photocatalytic reduction.[7] In 2010, Ye reported a novel semiconductor photocatalyst Ag_3PO_4, which exhibited strong photooxidative activities for O_2 evolution from water splitting in the presence of a sacrificial reagent $AgNO_3$, and a high degradation rate for organic dyes under visible-light irradiation.[8] The photocatalytic activity of Ag_3PO_4 is superior to those of previously reported visible-light photocatalysts, *e.g.*, $BiVO_4$ (ref. 8) and N-doped TiO_2.[9,10] Hence, it has been widely investigated.[11–16]

According to previously reported studies, the heterojunction structure between Ag_3PO_4 and other semiconductor materials may modulate the band gap, improve dispersion stability, and enhance the separation efficiency of photoelectron–hole pairs, leading to the enhanced photocatalytic activity of the composite catalyst. Several Ag_3PO_4-based composite photocatalysts have been developed, *e.g.*, AgX/Ag_3PO_4 (X = Cl, Br, and I),[17–19] Ag_3PO_4/TiO_2,[20,21] Ag_3PO_4/CeO_2,[22,23] Ag_3PO_4/WS_2,[24] Bi_2O_3/Ag_3PO_4,[25] $Ag_3PO_4/BiPO_4$,[26–28] $Ag_3PO_4/BiOBr$,[29] and $Ag_3PO_4/g\text{-}C_3N_4$.[30–32]

In this study, Ag_3PO_4 and Ag_3PO_4@HP photocatalysts were prepared by silver-ammonia- solution-assisted solution co-deposition. The core–shell structure and photocatalytic properties of Ag_3PO_4@HP were investigated in detail.

2. Experimental

2.1 Preparation

2.1.1 Preparation of Ag_3PO_4. First, $AgNO_3$ and KH_2PO_4 were separately dissolved in distilled water. Second, a $NH_3 \cdot H_2O$ solution was slowly added to the $AgNO_3$ solution under constant magnetic stirring, affording a silver ammonia solution, until the brown precipitate disappeared. Then, a KH_2PO_4 solution with a $Ag(NH_3)_2NO_3 : KH_2PO_4$ molar ratio of 1 : 3 was added into the silver ammonia solution under intense stirring for 5 min before standing for 10 min, and the precipitates were collected by centrifugation. The obtained precipitate was washed three times with absolute ethanol and distilled water, followed by drying at 80 °C for 30 min, affording Ag_3PO_4.

2.1.2 Preparation of Ag_3PO_4@HP. First, Ho_2O_3 was dissolved in nitric acid, affording a $Ho(NO_3)_3$ solution. Second, the $Ho(NO_3)_3$ solution was mixed with the silver ammonia solution in a molar ratio of $Ho/Ag/PO_4^{3-}$ at $x/3{-}x/1$ ($x = 0.01, 0.05, 0.1,$ and 0.5). The next steps were the same as those for the preparation of Ag_3PO_4. The prepared Ag_3PO_4@HP samples were denoted as 1-Ag_3PO_4@HP, 2-Ag_3PO_4@HP, 3-Ag_3PO_4@HP, and 4-Ag_3PO_4@HP, corresponding to x values of 0.01, 0.05, 0.1, and 0.5, respectively.

2.2 Photocatalytic activity experiments

Photocatalytic activity experiments were carried out in a photoreactor at room temperature. BL-GHX-V Xe lamp with a 500 W electric power was used as the light source to simulate sunlight. The reaction solution included 30 mL of a rhodamine B, dahlia B, or methylthionine chloride solution, with an initial concentration of 5 mg L^{-1}, along with 0.05 g of the photocatalyst, respectively. First, the suspensions were stirred in the dark for 30 min to attain the adsorption–desorption equilibrium. After irradiation was started, the reaction solution was removed and immediately filtered after every 15 min. The reaction solution

---

[a] *Key Lab for Advanced Ceramics and Machining Technology of Ministry of Education, School of Materials Science and Engineering of Tianjin University, Tianjin, China. E-mail: lizhihongtju@163.com*

[b] *Key Laboratory of Inorganic Nonmetallic Materials of Hebei Province, Key Laboratory of Environment Functional Materials of Tangshan City, North China University of Science and Technology, Tangshan, Hebei, China*

[c] *Light Alloy Research Institute, Central South University, Changsha, Hubei, China*

concentration was measured by UV-Vis spectroscopy to evaluate the residual efficiency of the reaction solution. The residual efficiency can be calculated by the following equation, $\eta = C/C_0$, where C_0 (mg L^{-1}) is the initial concentration of the reaction solution before illumination, C is the concentration of the reaction solution (mg L^{-1}) after a certain illumination time (min), which is proportional to the absorbance.

2.3 Characterization

X-ray diffraction (XRD) patterns were recorded on a XRD instrument (BDX3200) with CuK_α radiation. The morphology images and energy-dispersive X-ray (EDX) spectra of the samples were obtained by field-emission scanning electron microscopy (FE-SEM, S-4800). Transmission electron microscopy (TEM) and high-resolution transmission electron microscopy (HRTEM) images were recorded on a TEM (FEI F30) instrument. Binding energy (BE) was analyzed on a Perkin-Elmer PHI-1600 X-ray photoelectron spectroscopy (XPS) system, which was calibrated using adventitious carbon (C 1s) as the reference peak. Photoluminescence (PL) and afterglow curves were recorded on a Hitachi F-7000 fluorescence spectrophotometer (Japan) equipped with a 450 W Xe lamp as the excitation light source. UV-Vis diffuse reflectance spectra (UV-Vis DRS) were obtained on a UV-Vis spectrometer (Puxi, UV1901), with an integral sphere, using $BaSO_4$ as the reference in the measurement range from 220 nm to 800 nm.

3. Results and discussion

3.1 Structural characterization

Fig. 1 shows the XRD patterns of Ag_3PO_4@HP and Ag_3PO_4. All of the diffraction peaks for as-prepared Ag_3PO_4 were indexed to the cubic phase of Ag_3PO_4 (JCPDS card 06-0505, Fig. 1). The XRD pattern of PH did not exhibit strong diffraction peaks, indicative of poor crystallinity. At low Ho^{3+} concentrations ($x \leq 0.1$), nearly no impurity peaks were observed for Ag_3PO_4@HP, and no obvious shift in the diffraction peaks was observed compared to those observed for pure Ag_3PO_4. The values of the lattice parameter a were 6.0190, 6.0154, 6.0194, and 6.0190 for the samples 1-Ag_3PO_4@HP to 4-Ag_3PO_4@HP, respectively, indicating that low Ho^{3+} concentrations almost do not affect the crystal lattice parameters of Ag_3PO_4. However, with the increase in the Ho/Ag molar ratio to 0.5/2.5, the strength of diffraction peaks significantly decreased, suggesting that Ho^{3+} does not enter the crystal lattice of Ag_3PO_4, but forms a new compound phase HP.

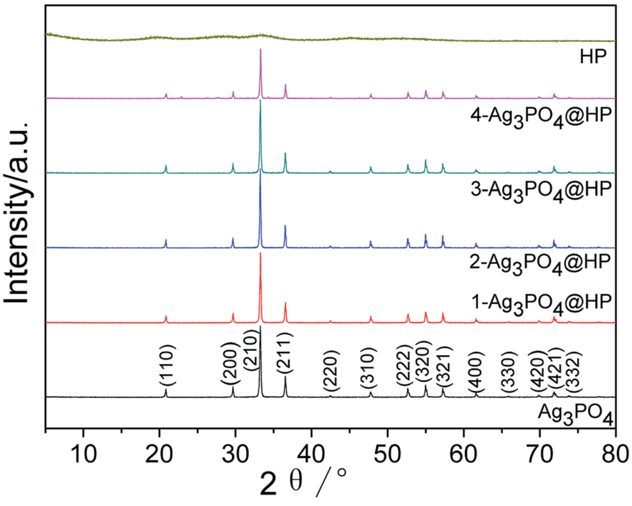

Fig. 1 XRD patterns of Ag_3PO_4, HP and Ag_3PO_4@HP with the mole ratio of Ho/Ag at 0.01 : 2.99, 0.05 : 2.95, 0.1 : 2.9, 0.5 : 2.5.

Fig. 2 shows the FE-SEM images of Ag_3PO_4 and Ag_3PO_4@HP. Without the introduction of Ho^{3+}, globular Ag_3PO_4 particles were primarily observed with sizes ranging from 200 to 300 nm (Fig. 2a). However, at a Ho/Ag molar ratio of 0.05/2.95, regular cubes were observed for Ag_3PO_4 particles, with sizes increasing to 300–400 nm (Fig. 2b). Ag_3PO_4 particles were coated by a thin layer of a flocculent amorphous substance HP, which was clearly observed at the junction of two neighboring particles; this observation was further confirmed from the TEM and HRTEM results (Fig. 4c and d). The crystalline-phase structure of the Ag_3PO_4 particles was distinctly improved, growing under the action of a thin layer of HP. As shown in Fig. 2c, with the increase in the Ho/Ag molar ratio to 0.1/2.9, the amount of flocculent amorphous substance HP rapidly increased. In Fig. 2c, the Ag_3PO_4 particle surface was surrounded by HP, making the shape of the Ag_3PO_4 particles irregular. Moreover, with the increase in the Ho/Ag molar ratio to 0.5/2.5, Ag_3PO_4 particles were fully encapsulated in the massive HP, and the size of the Ag_3PO_4 particles decreased to 100–200 nm.

EDX elemental mapping images were also recorded for further confirming the 2-Ag_3PO_4@HP composite structure. The elemental mapping images of silver, phosphorus, and oxygen exhibited similar shape as well as location (Fig. 3), confirming the existence of Ag_3PO_4 in the composite. The mapping of Ho revealed that Ho is well distributed in the sample, indicative of the presence of holmium. Furthermore, the mapping density of Ag on the surface was clearly greater than that of the other elements, which is possible for providing more photoelectrons for photocatalysis.

Fig. 4 shows the TEM and HRTEM images of the Ag_3PO_4 and 2-Ag_3PO_4@HP samples. The size of the predominantly globular Ag_3PO_4 particles was ~200–300 nm, and Ag_3PO_4 particles exhibited a smooth surface with few edges and corners, but there was serious aggregation (Fig. 4a). As shown in Fig. 4b, Ag_3PO_4 particles presented a cubic shape with a mean size of ~350 nm. The sharp edges and corners of the Ag_3PO_4 particles significantly increased. It is because that a small amount of the HP flocculent amorphous substance was generated on the surface or in the vicinity of the Ag_3PO_4 particles, improving the dispersion of Ag_3PO_4 particles and permitting the unrestricted growth of Ag_3PO_4 particles into cubes. This result is consistent with FE-SEM results. The specific surface areas of Ag_3PO_4 and Ag_3PO_4@HP were estimated as 3 $m^2\ g^{-1}$ and 11 $m^2\ g^{-1}$, respectively. The higher specific surface area of Ag_3PO_4@HP is related to the amorphous structure of HP and the improved dispersion of Ag_3PO_4.

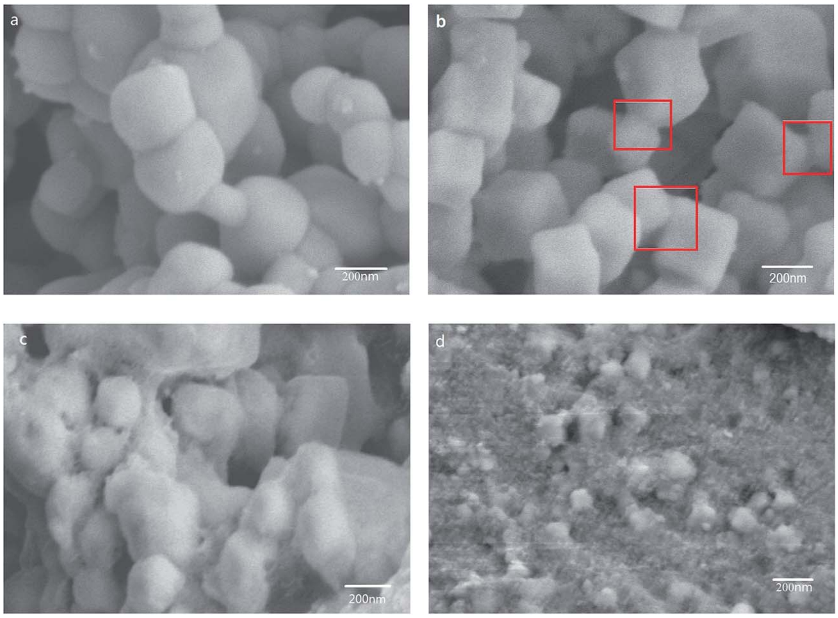

Fig. 2 FE-SEM images of Ag_3PO_4 (a) and Ag_3PO_4@HP with the mole ratio of Ho/Ag at 0.05 : 2.95 (b), 0.1 : 2.9 (c), 0.5 : 2.5 (d).

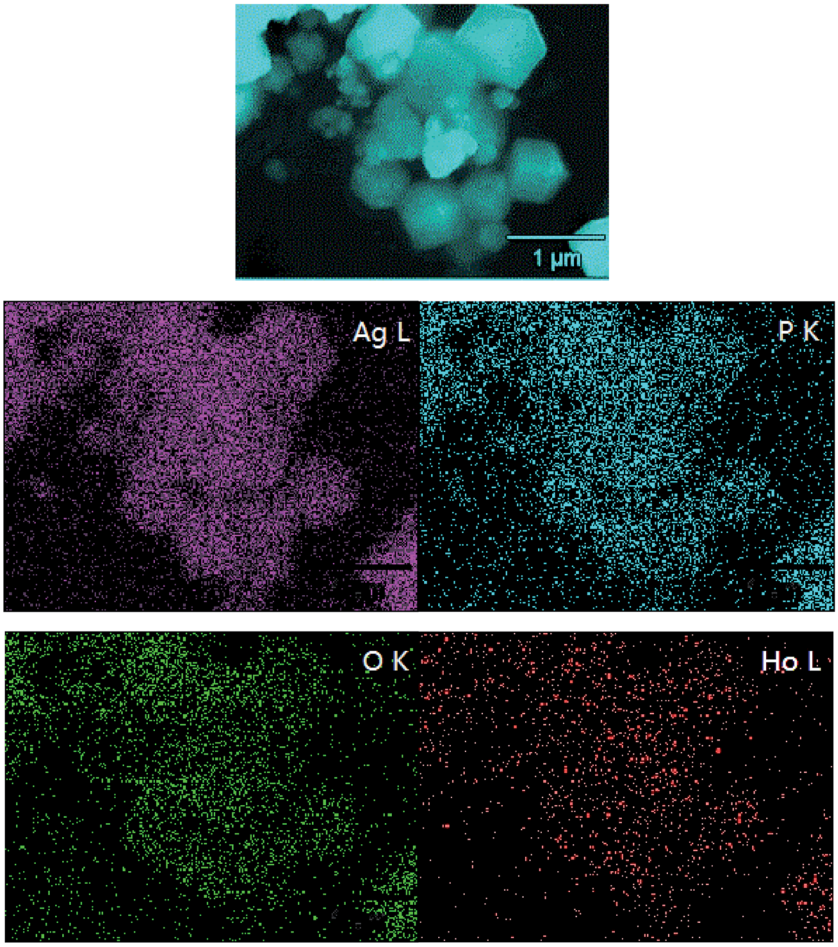

Fig. 3 EDX elemental mapping images of 2-Ag_3PO_4@HP with the mole ratio of Ho/Ag at 0.05 : 2.95.

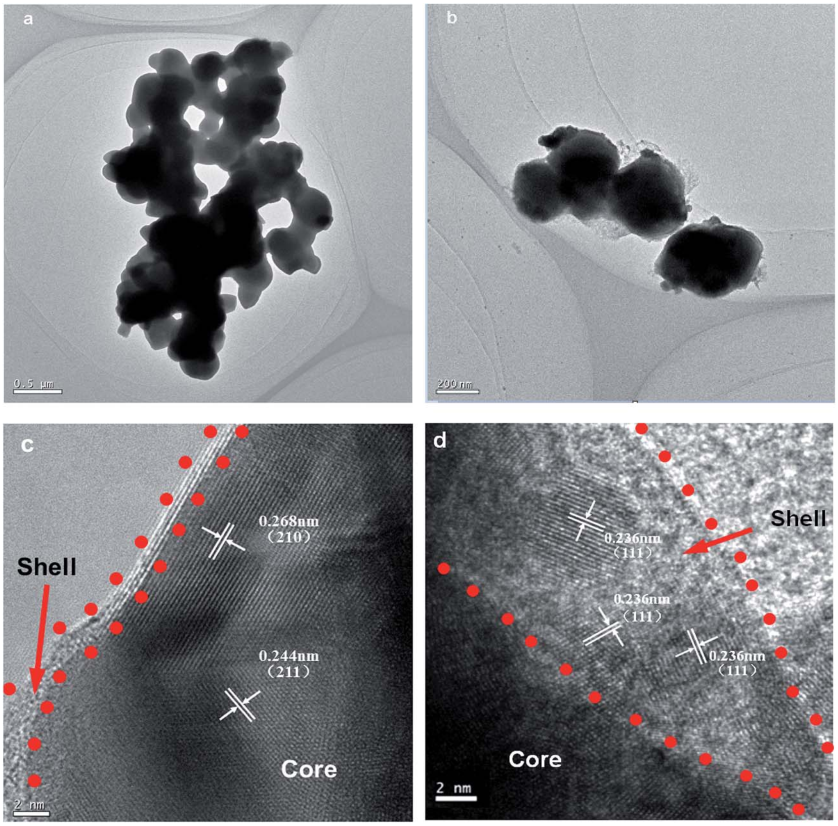

Fig. 4 TEM images of Ag_3PO_4 (a) and 2-Ag_3PO_4@HP (b) and HRTEM of 2-Ag_3PO_4@HP (c, d) with the mole ratio of Ho/Ag at 0.05 : 2.95.

In the HRTEM image shown in Fig. 4a, c and d crystalline lattice structure for 2-Ag_3PO_4@HP was clearly observed. As shown in Fig. 4c and d, Ag_3PO_4 particles were further confirmed to be encapsulated by an HP layer, affording the Ag_3PO_4@HP core–shell composite. The shell layer of the HP amorphous material was distinctly different from the Ag_3PO_4 core, and the thickness of the shell layer was approximately 2–10 nm. Lattice spacings of 0.27 and 0.24 nm were observed, corresponding to the (210) and (211) planes of Ag_3PO_4, respectively. Interestingly, as shown in Fig. 4d, some small particles with sizes of 4–5 nm were crystallized in the thicker HP shell. The lattice spacing of these small particles was 0.236 nm, corresponding to the (111) planes of Ag^0. Ag^0 is possibly produced by the reduction of Ag^+, owing to daylight illumination during preparation.[21] The reaction can be proposed as shown in eqn (1):

$$2AgNO_3 = 2Ag + 2NO_2\uparrow + O_2\uparrow \quad (1)$$

Fig. 5a shows the full-scan XPS spectra of Ag_3PO_4 and 2-Ag_3PO_4@HP: all elements (Ag(b), O(c), P(d), and Ho(e)) were observed in 2-Ag_3PO_4@HP, among which Ho was only observed in Ag_3PO_4@HP. Fig. 5b shows the Ag 3d spectra of Ag_3PO_4 and Ag_3PO_4@HP samples: Two characteristic BE peaks were observed at 367.7/373.9 eV and 367.6/373.8 eV, attributed to Ag $3d_{5/2}$ and Ag $3d_{3/2}$ bands, respectively. After the peak fitting of O 1s, two sets of binding energy at 530.6/532.7 eV and 530.4/532.5 eV, corresponding to Ag_3PO_4 and Ag_3PO_4@HP samples, respectively (Fig. 5c). Two peaks corresponded to the crystal lattice oxygen and surface hydroxyl groups, respectively. The P 2p peaks of 2-Ag_3PO_4@HP and Ag_3PO_4 were observed at 133.2 and 132.8 eV, respectively (Fig. 5d); both peaks were assigned to the sample lattice P^{5+}. Compared with that corresponding to Ag_3PO_4, the P 2p peak of 2-Ag_3PO_4@HP slightly shifted to higher BE, indicating that P 2p on the Ag_3PO_4 surface undergoes a different chemical reaction from the inside, which is the formation of the HP shell. A BE peak was observed at 163.1 eV in the XPS spectrum for Ho (Fig. 5e), corresponding to Ho $^4d_{5/2}$. This result further indicated the presence of Ho as Ho^{3+} in the composite.

Fig. 6 shows the UV-Vis DRS spectra of Ag_3PO_4 and 2-Ag_3PO_4@HP. Absorption edges of Ag_3PO_4 and Ag_3PO_4@HP were observed in the visible region (Fig. 6a), and considerable absorption was observed in the visible spectrum in the range of ~200–530 nm. $HoPO_4$ exhibited strong absorption in the UV region (<350 nm). In addition, some sharp absorption peaks were observed in the visible range of HP, related to the characteristic absorption of Ho^{3+}. Absorption peaks were observed at 421 nm, 447 nm, 457 nm, 477 nm, 540 nm, and 642 nm, corresponding to the energy-level transitions of Ho^{3+}, $^5G_5 \rightarrow {}^5I_8$, $^5G_0(^5F_1) \rightarrow {}^5I_8$, $^5G_6 \rightarrow {}^5I_8$, $^5F_3 \rightarrow {}^5I_8$, $^5S_2(^5F_4) \rightarrow {}^5I_8$, and $^5F_5 \rightarrow {}^5I_8$, respectively. The direct band gaps of Ag_3PO_4 and HP were obtained from the plot of $(\alpha h\nu)^2$ *versus* $h\nu$, which were 2.42 eV and 3.50 eV, respectively (Fig. 6b).

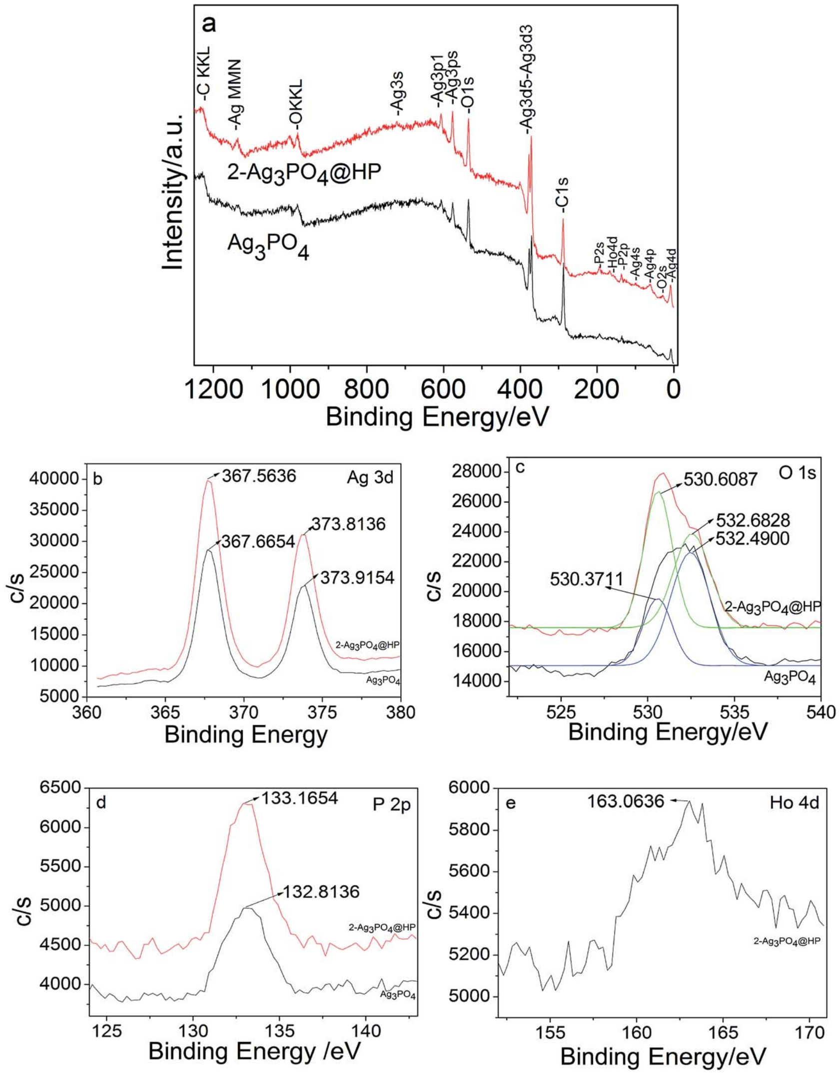

Fig. 5 The XPS results images of Ag_3PO_4 and 2-Ag_3PO_4@HP with the mole ratio of Ho/Ag at 0.05 : 2.95.

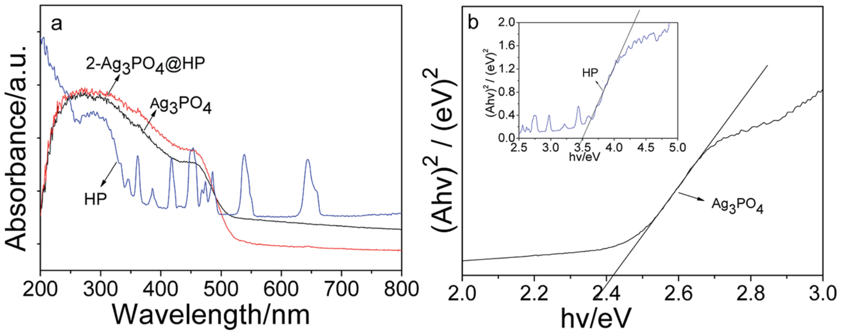

Fig. 6 UV-Vis diffuse reflection spectrum of Ag_3PO_4, HP and Ag_3PO_4@HP.

3.2 Photocatalytic activity

Fig. 7(a–c) show the photocatalytic degradation of rhodamine B, dahlia B, and methylthionine chloride using Ag_3PO_4, HP, and Ag_3PO_4@HP under sunlight irradiation, respectively. Ag_3PO_4 and Ag_3PO_4@HP samples almost degraded the three dyes within 45 min with different degradation rates, but HP marginally affected the degradation of all dyes. From the comparison of the photocatalytic experimental results, at a Ho : Ag molar ratio of less than 0.1 : 2.9, the photocatalytic activity of Ag_3PO_4@HP was typically greater than that of pure Ag_3PO_4. After irradiation for 30 min, 2-Ag_3PO_4@HP exhibited

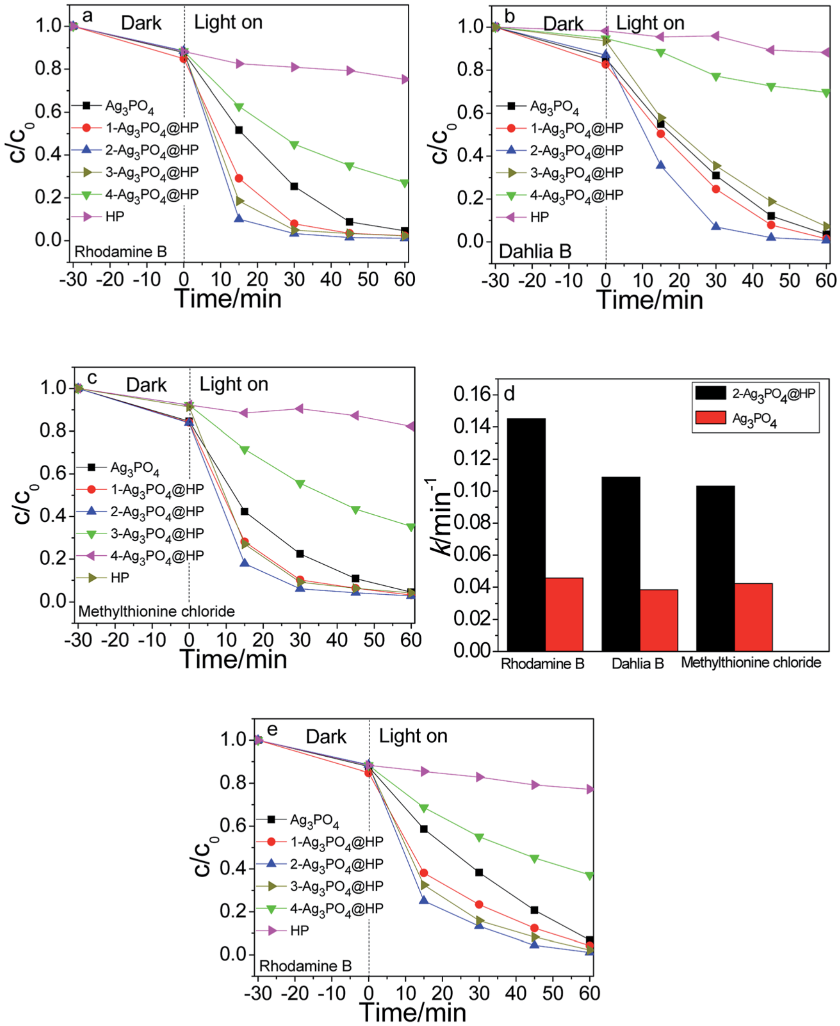

Fig. 7 The photocatalytic degradation results of Ag_3PO_4, HP and Ag_3PO_4@HP. The degradation results of rhodamine B (a), dahlia B (b), and methylthionine chloride (c); the values of the reaction rate constant k (d) of the photocatalytic degradation; the visible-light photocatalytic activities (e) in the degradation of rhodamine B, using a Xe-lamp with a 420 nm cutoff filter.

the best degradation rates of 96.70%, 93.05%, and 93.98% for rhodamine B, dahlia B, and methylthionine, respectively, while the corresponding degradation rates for Ag_3PO_4 were 74.66%, 69.11%, and 77.58%, calculated from the data shown in Fig. 7(a–c). Generally, the photocatalytic activity of Ag_3PO_4 fits the first-order kinetics. According to the first-order kinetics ($\ln(C_0/C) = kt$), the reaction rate constant k can be calculated (Fig. 7d). The k values for rhodamine B, dahlia B, and methylthionine chloride using 2-Ag_3PO_4@HP were 0.1251 min^{-1}, 0.1088 min^{-1}, and 0.10317 min^{-1}. These values were 3.1, 2.8, and 2.4 times greater than that of pure Ag_3PO_4, respectively.

Fig. 7e shows the visible-light photocatalytic activities of Ag_3PO_4 and Ag_3PO_4@HP for the degradation of rhodamine B using a Xe lamp with a 420 nm cutoff filter. After irradiation for 30 min, the degradation rates of rhodamine B for Ag_3PO_4, 1-Ag_3PO_4@HP, ∼4-Ag_3PO_4@HP, and HP were 56.30%, 72.50%, 84.97%, 81.99%, 37.62%, and 6.07%, respectively. 2-Ag_3PO_4@HP still exhibited better visible-light photocatalytic activity compared to the other tested photocatalysts.

In addition, the cycling stability of photocatalysts is an important property for practical applications. Hence, the stability of 2-Ag_3PO_4@HP was examined in terms of the recycling degradation of a rhodamine B solution under sunlight irradiation. As shown in Fig. 8a, after five recycling runs, 2-Ag_3PO_4@HP completely degraded the reaction solution with a concentration of 5 mg L^{-1} in 60 min, suggesting a high recycling stability for 2-Ag_3PO_4@HP. To evaluate the structural stability, the crystalline structures of Ag_3PO_4 and Ag_3PO_4@HP before and after recycling experiments were examined (Fig. 8b). No diffraction peaks corresponding to metallic Ag were observed in the unused photocatalyst samples. However, metallic Ag was observed in the HRTEM images of unused 2-Ag_3PO_4@HP (Fig. 4d), possibly because of the low amount of the metallic Ag, resulting in the absence of the XRD diffraction peaks of Ag. After five recycling runs, diffraction peaks corresponding to metallic Ag were clearly observed in the XRD pattern of pure Ag_3PO_4 at $2\theta = 38.115°$ and $44.299°$, indicating that Ag_3PO_4 is partially reduced into metallic Ag particles during

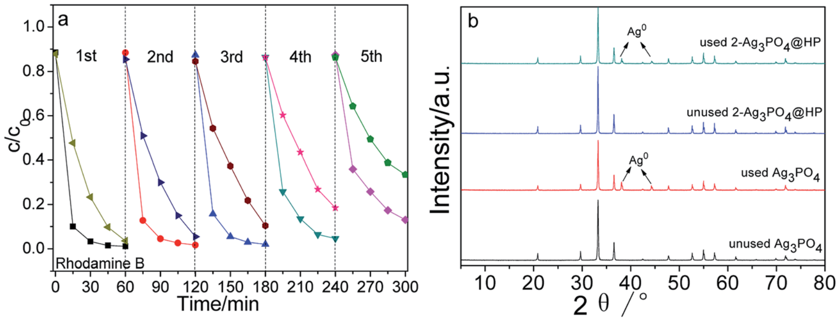

Fig. 8 Recycling runs of Ag_3PO_4 and 2-Ag_3PO_4@$HoPO_4$ samples in the degradation of rhodamine B.

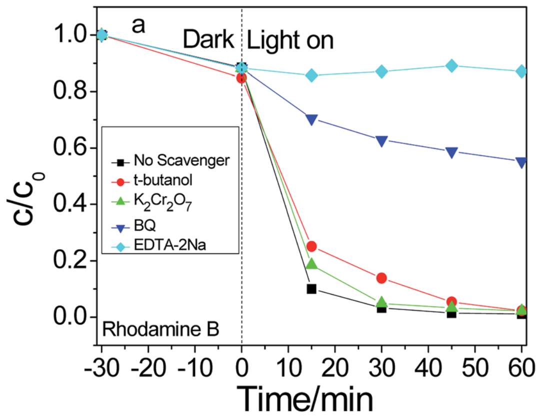

Fig. 9 Photodegradation efficiency of rhodamine B with 2-Ag_3PO_4@HP as photocatalyst under different scavengers.

photocatalytic degradation. Compared to the XRD pattern of pure Ag_3PO_4, smaller diffraction peaks corresponding to metallic Ag were observed in the XRD pattern of 2-Ag_3PO_4@HP after five recycling runs, indicating that the HP shell enhances the stability of Ag_3PO_4.

3.3 Possible photocatalytic mechanism

To examine the reactive species, scavenging experiments were carried out to elucidate the possible pathway or mechanism for photocatalytic degradation. To probe different reactive species during the photocatalysis of Ag_3PO_4@HP systems, *t*-butanol, benzoquinone (BQ), EDTA-2Na, and potassium dichromate ($K_2Cr_2O_7$) were separately added to the RhB solutions as the scavengers ([scavenger] = 0.3 mmol L^{-1}) for hydroxyl radicals ($\cdot OH^-$), superoxide radicals ($^{\bullet}O_2$), holes (h^+), and electrons (e^-), respectively (Fig. 9). $K_2Cr_2O_7$ negligibly affected the photodegradation rates of RhB. The results indicated that e^- do not appear to be the main reactive species during photocatalysis. The addition of EDTA–2Na and BQ caused the rapid termination of photocatalysis, indicating that the photogenerated h^+ and $^{\bullet}O_2$ possibly play a crucial role during the photocatalytic degradation of RhB. The contribution of the reactive species for photocatalytic degradation follows the order of $h^+ > {}^{\bullet}O_2 > {}^{\bullet}OH^- > e^-$.

Considering the energy-band structure theory, a previous study,[33] and structural and performance characteristics, a possible energy-band structure model was proposed for improving the photocatalytic activity and stability of the Ag_3PO_4@HP heterostructures, as shown in Fig. 10. The valence-band (VB) and conduction-band (CB) potentials of Ag_3PO_4 can be calculated by the following empirical formula (as shown in eqn (2) and (3), respectively), where X is the Mulliken electronegativity ($X_{HP} \cong 6.3205$ eV), E_e is the energy of free electrons on the hydrogen scale ($E_e \cong 4.5$ eV), and E_g is the bandgap ($E_g = 3.5$ eV). Therefore, the VB and CB potentials of HP were calculated as 3.44 eV and −0.06 eV, respectively.

$$E_{VB} = X - E_e + 0.5E_g \quad (2)$$

$$E_{CB} = E_{VB} - E_g \quad (3)$$

Under Xe lamp irradiation, both Ag_3PO_4 and HP were excited, and the photogenerated electrons and holes were simultaneously created. The CB potential (0.45 eV) of Ag_3PO_4 was lower than that of HP (−0.06 eV), and the VB potential (2.89 eV) was greater than that of HP (3.44 eV). Thus, the photogenerated electrons and holes spontaneously shift from HP to Ag_3PO_4. Simultaneously, the photogenerated electrons rapidly migrate from the CB of Ag_3PO_4 to the Ag nanoparticles *via* the Schottky barrier. Ag nanoparticles on the Ag_3PO_4 surface acted as a sink for electrons, these electrons reacted with the adsorbed O_2 to generate the active ion species ($^{\bullet}O^{2-}$). This process

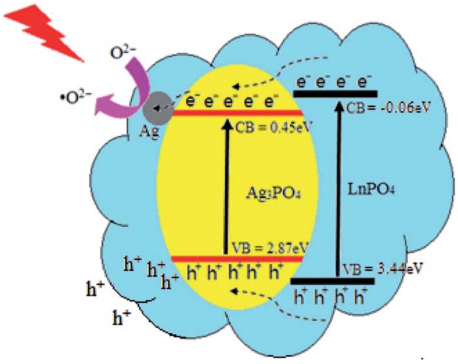

Fig. 10 The photocatalytic mechanism model of Ag_3PO_4@HP.

promoted the separation of the photogenerated electron–hole pairs. However, the holes (h^+) in the VB of Ag_3PO_4 were directly transferred to the organic dye surface for further reaction. Thus, this photocatalytic system, consisting of $LnPO_4$, Ag nanoparticles, and Ag_3PO_4, may be more effective for the degradation of organic pollutants.

In addition, the higher specific surface area of Ag_3PO_4@HP was crucial for enhancing the photocatalytic activity of Ag_3PO_4, related to the more efficient adsorption of the dye molecules. Therefore, the high photocatalytic activity of Ag_3PO_4@HP is believed to be related to the combination of two effects.

4. Conclusions

In this study, Ag_3PO_4@Ag_3PO_4@HP composite photocatalysts were prepared by silver-ammonia-solution-assisted solution co-deposition. The core–shell structure of the Ag_3PO_4@HP composite significantly improved the photocatalytic activity of Ag_3PO_4.

Acknowledgements

The project was supported by the National Natural Science Fund of China (Grant No. 51572069).

References

1 A. Fujishima and K. Honda, Electrochemical photocatalysis of water at semiconductor electrode, *Nature*, 1972, **238**, 53–58.

2 R. Asahi, T. Morikawa, T. Ohwaki, K. Aoki and Y. Taga, Visible-light photocatalysis in nitrogen-doped titanium oxides, *Science*, 2001, **293**, 269–271.

3 M. Z. Ge, C. Y. Cao, J. Y. Huang, S. H. Li, Z. Chen, K. Q. Zhang, S. S. Aldeyab and Y. K. Lai, A review of one-dimensional TiO_2 nanostructured materials for environmental and energy applications, *J. Mater. Chem. A*, 2016, **4**, 6772–6801.

4 S. Obregón and G. Colón, On the origin of the photocatalytic activity improvement of $BiVO_4$ through rare earth tridoping, *Appl. Catal., A*, 2015, **501**, 56–62.

5 X. F. Zhang, B. Y. Zhang, K. Cao, J. Brillet, J. Y. Chen, M. K. Wang and Y. Shen, Perovskite Solar Cell-TiO_2@$BiVO_4$ Photoelectrochemical System for Direct Solar Water Splitting, *J. Mater. Chem. A*, 2015, **3**, 21630–21636.

6 T. A. Kandiel, A. Y. Ahmed and D. Bahnemann, TiO_2(B)/anatase heterostructure nanofibers decorated with anatase nanoparticles as efficient photocatalysts for methanol oxidation, *J. Mol. Catal. A: Chem.*, 2016, **425**, 55–60.

7 H. K. Jin, G. Magesh, H. J. Kang, M. Banu, H. K. Ju, J. Lee and J. S. Lee, Carbonate-coordinated cobalt co-catalyzed $BiVO_4$/WO_3 composite photoanode tailored for CO_2 reduction to fuels, *Nano Energy*, 2015, **15**, 153–163.

8 Z. G. Yi, J. H. Ye, N. Kikugawa, T. Kako, S. Ouyang, H. Stuartwilliams, H. Yang, J. Cao, W. Luo and Z. Li, An orthophosphate semiconductor with photooxidation properties under visible-light irradiation, *Nat. Mater.*, 2010, **9**, 559–564.

9 Y. Bi, H. Hu, Z. Jiao, H. Yu, G. Lu and J. Ye, Two-dimensional dendritic Ag_3PO_4 nanostructures and their photocatalytic properties, *PCCP*, 2012, **14**, 14486–14488.

10 Y. Bi, H. Hu, S. Ouyang, G. Lu, J. Cao and J. Ye, Photocatalytic and photoelectric properties of cubic Ag_3PO_4 sub-microcrystals with sharp corners and edges, *Cheminform*, 2012, **43**, 3748–3750.

11 W. Y. Lin, S. J. Zhang, D. Y. Wang, C. X. Zhang and D. L. Sun, Ultrasound-assisted synthesis of high-efficiency Ag_3PO_4/CeO_2 heterojunction photocatalyst, *Ceram. Int.*, 2015, **41**, 8956–8963.

12 C. Wang, J. X. Zhu, X. Y. Wu, H. Xu, Y. H. Song, J. Yan, Y. X. Song, H. Y. Ji, K. Wang and H. M. Li, Photocatalytic degradation of bisphenol A and dye by graphene-oxide/Ag_3PO_4 composite under visible light irradiation, *Ceram. Int.*, 2014, **40**, 8061–8070.

13 U. Sulaeman, F. Febiyanto, S. Yin and T. Sato, The highly active saddle-like Ag_3PO_4 photocatalyst under visible light irradiation, *Catal. Commun.*, 2016, **85**, 22–25.

14 Q. Wu, P. F. Wang, F. T. Niu, C. P. Huang, Y. Li and W. F. Yao, A novel molecular sieve supporting material for enhancing activity and stability of Ag_3PO_4 photocatalyst, *Appl. Surf. Sci.*, 2016, **378**, 552–563.

15 S. S. Patil, D. R. Patil, S. K. Apte, M. V. Kulkarni, J. D. Ambekar, C. J. Park, S. W. Gosavi, S. S. Kolekar and B. B. Kale, Confinement of Ag_3PO_4 nanoparticles supported by surface plasmon resonance of Ag in glass: efficient nanoscale photocatalyst for solar H_2 production from waste H_2S, *Appl. Catal., B*, 2016, **190**, 75–84.

16 Q. H. Xiang, L. Di, T. T. Shen and L. Fan, Graphene-modified nanosized Ag_3PO_4 photocatalysts for enhanced visible-light photocatalytic activity and stability, *Appl. Catal., B*, 2015, **162**, 196–203.

17 P. Amornpitoksuk and S. Suwanboon, Photocatalytic decolorization of methylene blue dye by Ag_3PO_4–AgX(X = Cl^-, $Br^-$and I^-) under visible light, *Adv. Powder Technol.*, 2014, **25**, 1026–1030.

18 J. Cao, B. Luo, H. Lin, B. Xu and S. Chen, Visible light photocatalytic activity enhancement and mechanism of AgBr/Ag_3PO_4 hybrids for degradation of methyl orange, *J. Hazard. Mater.*, 2012, **217–218**, 107–115.

19 H. Katsumata, T. Hayashi, M. Taniguchi, T. Suzuki and S. Kaneco, AgI/Ag_3PO_4 hybrids with highly efficient visible-light driven photocatalytic activity, *Mater. Res. Bull.*, 2015, **63**, 116–122.

20 W. F. Yao, B. Zhang, C. P. Huang, C. Ma, X. L. Song and Q. J. Xu, Synthesis and characterization of high efficiency and stable Ag_3PO_4/TiO_2 visible light photocatalyst for the degradation of methylene blue and rhodamine B solutions, *J. Mater. Chem.*, 2012, **22**, 4050–4055.

21 C. N. Tang, E. Z. Liu, J. Fan, X. Y. Hu, L. M. Kang and J. Wan, Heterostructured Ag_3PO_4/TiO_2 nano-sheet film with high efficiency for photodegradation of methylene blue, *Ceram. Int.*, 2014, **40**, 15447–15453.

22 Z. M. Yang, G. F. Huang, W. Q. Huang, J. M. Wei, X. G. Yan, Y. Y. Liu, C. Jiao, Z. Wan and A. Pan, Novel Ag_3PO_4/CeO_2 composite with high efficiency and stability for photocatalytic applications, *J. Mater. Chem. A*, 2014, **2**, 1750–1756.

23 W. Y. Lin, S. J. Zhang, D. Y. Wang, C. X. Zhang and D. L. Sun, Ultrasound-assisted synthesis of high-efficiency Ag_3PO_4/CeO_2 heterojunction photocatalyst, *Ceram. Int.*, 2015, **41**, 8956–8963.

24 H. J. Yu, Y. Yu, J. H. Liu, P. Y. Ma, Y. C. Wang, F. Zhang and Z. Y. Fu, Space-confined growth of Ag_3PO_4 nanoparticles within WS_2 sheets: Ag_3PO_4/WS_2 composites as visible-light-driven photocatalysts for decomposing dyes, *J. Mater. Chem. A*, 2015, **3**, 19439–19444.

25 F. Ding, S. Z. Zhang, X. G. Luo and X. Y. Lin, Fabrication of $Ag_3PO_4/\alpha\text{-}Bi_2O_3$ composites with enhanced photocatalytic properties under visible light, *RSC Adv.*, 2015, **5**, 96685–96694.

26 N. Mohaghegh, M. Tasviri, E. Rahimi and M. Gholami, A novel p–n junction $Ag_3PO_4/BiPO_4$-based stabilized Pickering emulsion for highly efficient photocatalysis, *RSC Adv.*, 2015, 12944–12955in press.

27 Y. G. Lv, K. Huang, W. Zhang, B. Yang, F. L. Chi, S. L. Ran and X. G. Liu, One step synthesis of $Ag/Ag_3PO_4/BiPO_4$ double-heterostructured nanocomposites with enhanced visible-light photocatalytic activity and stability, *Ceram. Int.*, 2014, **40**, 8087–8092.

28 S. Y. Wu, H. Zheng, Y. Y. Wu, W. Lin, T. Z. Xu and M. Guan, Hydrothermal synthesis and visible light photocatalytic activity enhancement of $BiPO_4/Ag_3PO_4$ composites for degradation of typical dyes, *Ceram. Int.*, 2014, **40**, 14613–14620.

29 O. Mehraj, N. A. Mir, B. M. Pirzada and S. Sabir, Fabrication of novel Ag_3PO_4/BiOBr heterojunction with high stability and enhanced visible-light-driven photocatalytic activity, *Appl. Surf. Sci.*, 2015, **332**, 419–429.

30 S. Kumar, T. Surendar, A. Baruah and V. Shanker, Synthesis of a novel and stable $g\text{-}C_3N_4\text{–}Ag_3PO_4$ hybrid nanocomposite photocatalyst and study of the photocatalytic activity under visible light irradiation, *J. Mater. Chem. A*, 2013, **1**, 5333–5340.

31 J. F. Zhang, J. L. Lv, K. Dai, Q. Liu, C. H. Liang and G. P. Zhu, Facile and green synthesis of novel porous $g\text{-}C_3N_4/Ag_3PO_4$ composite with enhanced visible light photocatalysis, *Ceram. Int.*, 2016, **43**, 1522–1529.

32 L. Li, Y. H. Qi, J. R. Lu, S. L. Lin, W. J. An, Y. H. Liang and W. Q. Cui, A stable $Ag_3PO_4@g\text{-}C_3N_4$ hybrid core@shell composite with enhanced visible light photocatalytic degradation, *Appl. Catal., B*, 2015, **183**, 133–141.

33 T. Y. Huang, Y. J. Chen, C. Y. Lai, *et al.* Synthesis, characterization, enhanced sunlight photocatalytic properties, and stability of Ag/Ag_3PO_4 nanostructure-sensitized $BiPO_4$[J], *RSC Adv.*, 2015, **5**, 43854–43862.